

## Facile Integration between Si and Catalyst for High-Performance Photoanodes by a Multifunctional Bridging Layer

Beidou Guo,<sup>‡,§,†</sup> Aisha Batool,<sup>‡,§,†</sup> Guancai Xie,<sup>‡,§</sup> Rajender Boddula,<sup>‡</sup> Liangqiu Tian,<sup>‡,§</sup>

Saad Ullah Jan,<sup>‡,§</sup> and Jian Ru Gong<sup>‡,\*</sup>

<sup>‡</sup>Chinese Academy of Sciences (CAS) Key Laboratory of Nanosystem and Hierarchy Fabrication, CAS  
Center for Excellence in Nanoscience, National Center for Nanoscience and Technology, Beijing  
100190, P. R. China

<sup>§</sup>University of CAS, *Beijing 100049, P. R. China*

\* gongjr@nanoctr.cn

### Experimental Details

The as-received commercial polycrystalline  $n^+p$ -Si composed of the  $n^+$ -Si emitter side with an anti-reflection  $\text{SiN}_x$  layer and the bare p-type side, was cleaved into the required pieces ( $1\text{ cm} \times 1.2\text{ cm}$ ) as the photoanode substrate. The textured surface of  $n^+p$ -Si has larger surface area, which is beneficial for increasing photoabsorption and catalyst load compared to the flat surface. The Ni metal film was deposited on the p-side surface of  $n^+p$ -Si at the rate of  $\sim 0.1\text{ \AA s}^{-1}$  in a thermal evaporation system, keeping the Si substrate temperature at  $150\text{ }^\circ\text{C}$ , after rinsed by acetone, isopropyl alcohol, and deionized water with ultrasonic agitation, each for 5 min, in succession. Immediately prior to Ni coating, the p-side of  $n^+p$ -Si was etched in buffered HF (10% in volume) for 20 s to remove the surface native oxide, rinsed with deionized water, blow-dried with  $\text{N}_2$  gas, fixed on the sample holder using the Kapton tape, and then loaded into the vacuum chamber of the thermal evaporator. After Ni deposition on the p-side surface of  $n^+p$ -Si, the silver electrodes at the back side were adhered to the transparent conducting oxide (TCO) coated glass, which acts as a transparent conductor for the PEC test, supports and protects the emitter against contacting with the solution, by rubbing the indium-gallium (InGa) eutectic.

To prepare the external circuit, one strip of copper tape was inserted into a polytetrafluoroethylene tube, and the other strip was fixed on the outer wall of this tube. The two strips of copper tapes were adhered to the TCO glass and the Ni film by InGa, as the electrical wires of working electrodes for the PEC test (WE1) and electrodeposition (WE2), respectively (Figure S1). After that, the entire assembly was encased by epoxy (Hysol 9460F) to avoid the leakage of the electrolyte, and 704 silica gel was used as a second protection layer on epoxy. The free ends of these two strips of copper tapes were used to connect power source to apply the external voltage.

The Ni metal film on the  $n^+p$ -Si/SiO<sub>x</sub>/Ni photoelectrode was activated by cycling the potential between -0.3 to 1.6 V versus the saturated calomel electrode (SCE) using the cyclic voltammetry (CV) measurement on the electrochemical workstation in 1.0 M KOH electrolyte at the sweep rate of 50 mV s<sup>-1</sup>, with a Pt sheet as a counter electrode, SCE as a reference electrode, and  $n^+p$ -Si/SiO<sub>x</sub>/Ni as a working electrode, under 1 Sun.

Finally, the NiFe-LDH nanoarray film was electrodeposited on the activated Ni film using the WE2 circuit. The electrocatalytic activity of NiFe-LDH as a co-catalyst on the activated Ni film was optimized by tuning the content ratio of Ni<sup>2+</sup> and Fe<sup>2+</sup> ions in the precursor solution and its film thickness. To this end, the solution with different stoichiometric molar ratios of Ni<sup>2+</sup> and Fe<sup>2+</sup> ions was prepared by dissolving nickel nitrate (Ni(NO<sub>3</sub>)<sub>2</sub> · 6H<sub>2</sub>O) and iron sulfate (FeSO<sub>4</sub> · 7H<sub>2</sub>O) molecular precursor salts in 100 ml of water under stirring in inert gas (Ar) atmosphere, to prevent the self-oxidation of Fe<sup>2+</sup> into Fe<sup>3+</sup>; while the total amount of ions (Ni<sup>2+</sup> and Fe<sup>2+</sup>) was kept to 0.15 mol. All the electrochemical depositions were carried out by applying the cathodic potential of -1.0 V versus SCE in the dark.

## Materials and Chemicals

The commercial polycrystalline  $n^+p$ -Si composed of the  $n^+$ -Si emitter side with an anti-reflection SiN<sub>x</sub> layer and the bare p-type side was acquired from LDK Solar Co., Ltd. Buffered hydrogen fluoride (10%, v/v), ethanol (AR, ≥ 99.7%), isopropyl alcohol (HPLC, ≥ 99.5%), indium-gallium (InGa) eutectics (Aldrich), 7640 adhesive, nickel nitrate (Ni(NO<sub>3</sub>)<sub>2</sub> · 6H<sub>2</sub>O) (99.999%, Guanghua Sci-Tech Co., Ltd), iron sulfate (FeSO<sub>4</sub> · 7H<sub>2</sub>O) (99.999 %, Xilong Scientific Co., Ltd.), and KOH (AR, 99%) were used as

received without further treatment. Ultrapure water (resistivity = 18 MΩ cm) used for preparing all solutions was obtained from a Milli-Q system.

### Characterizations

Scanning electron microscopy (SEM) images were obtained using a field-emission S4800 scanning electron microscope (FESEM, Hitachi, Japan) at an accelerating voltage of 10 kV. X-ray diffraction (XRD) patterns were obtained from X'pert powder diffractometer using CuKα radiations ( $\lambda = 0.15418$  nm) with an operating voltage of 40 kV and an operating current of 40 mA at the scan rate of  $0.05^\circ 2\theta$  s<sup>-1</sup> to characterize the structures of the films on the n<sup>+</sup>p-Si anode, where  $\lambda$  is the wavelength and  $\theta$  the Bragg's diffraction angle. A field-emission transmission electron microscope (FEI Technai F20) operated at 200 kV was used to further characterize the crystallographic structures under the mode of high-resolution transmission electron microscopy (HRTEM). X-ray photoelectron spectra (XPS) was performed in an ultrahigh vacuum VG ESCALAB 210 electron spectrometer equipped with a multi-channel detector. The spectra were excited using monochromatic Al Kα (1486.6 eV) source radiation. The depth profiling was performed using Auger electron spectroscopy (PHI-700 scanning Auger nanoprobe).

### Electrochemical measurements

All of the electrochemical measurements were performed in 1.0 M KOH (pH = 13.6) electrolyte solution in the three-electrode system on a Zahner Zennium electrochemical workstation in 1.0 M KOH electrolyte at the sweep rate of 50 mV s<sup>-1</sup>, with a Pt sheet as a counter electrode, SCE as a reference electrode, and n<sup>+</sup>p-Si/SiO<sub>x</sub>/Ni as a working electrode, under illumination with simulated air mass 1.5 global (AM 1.5G) sunlight generated from a 500 W Xenon lamp equipped with an AM 1.5G filter (CEL-S500, Au-light Co., Ltd.), and the light density was calibrated to be 100 mW cm<sup>-2</sup> (1 Sun). The same conditions were used to test the PEC properties of the photoanodes in this work. The cyclic voltammetry (CV) curves were recorded at the scan rate of 50 mV s<sup>-1</sup>. The electrochemical test using the p<sup>++</sup>-Si as a conducting substrate was performed in the dark. All measured potentials were converted from the saturated calomel electrode (SCE) to the reversible hydrogen electrode (RHE) reference scale using the following relationship:

$$E_{RHE} = E_{SCE} + 0.244 \text{ V} + 0.059 \times PH$$

### Faradaic efficiency

The measurement of the photoelectrochemically generated  $O_2$  from  $n^+p$ -Si/SiO<sub>x</sub>/Ni/NiO<sub>x</sub>/NiFe-LDH was held at a constant potential of 0.8 V versus RHE under illumination. Before the measurement, the electrolyte was thoroughly degassed by purging Ar gas for 30 min to ensure the absence of residual gas contaminants. The formation of  $O_2$  was detected by injecting the gas in the reactor headspace into a gas chromatograph (GC, 9790II) equipped with a semicapillary column and a thermal conductivity detector. The total  $O_2$  production including the  $O_2$  amount in the headspace and the dissolved  $O_2$  in the electrolyte was calculated by the ideal gas law. By comparing the theoretical  $O_2$  production calculated from the photocurrent to the actual  $O_2$  yield, the average Faradaic efficiency was obtained.

### Applied bias photon-to-current efficiency (ABPE)

The ABPE of the photoanode under illumination was calculated based on the current density versus potential (J-V) curve according to the following equation:<sup>1</sup>

$$ABPE = \frac{J \times (1.23 \text{ V} - E_{bias}) \times \eta_F}{P_{in}} \times 100\%$$

where,  $J$  is the photocurrent density ( $\text{mA cm}^{-2}$ ),  $E_{bias}$  is the calibrated applied bias potential related to the RHE,  $\eta_F$  is Faradaic efficiency, and  $P_{in}$  is the incident illumination power density.

### Electrochemical active surface area (ECSA)

The ECSA of our designed water oxidation systems was estimated from the electrochemical double-layer capacitance ( $C_{dl}$ ) of the  $n^+p$ -Si/SiO<sub>x</sub>/NiO<sub>x</sub> and  $n^+p$ -Si/SiO<sub>x</sub>/NiO<sub>x</sub>/NiFe-LDH electrodes.  $C_{dl}$  was determined by measuring the scan-rate ( $\nu$ ) dependent electrochemical capacitive current associated with the double-layer charging in the non-Faradaic potential region, by using the cyclic voltammetry (CV) measurement.<sup>2</sup> The plot of these calculated charging current ( $I_c = I_{anodic} - I_{cathodic}$ ) in the middle of the applied potential domain as a function of  $\nu$ , yielded a linear slope equivalent to twice of the double-layer capacitance  $C_{dl}$  and was used to represent ECSA of these catalysts. For these measurements, CV curves were run at multiple scan rates of 20, 40, 60, 80, and 100  $\text{mV s}^{-1}$ .

### Mott-Schottky (MS) analysis

The differential capacitance-potential data of the  $n^+p$ -Si/SiO<sub>x</sub>/Ni/NiO<sub>x</sub> and  $n^+p$ -Si/SiO<sub>x</sub>/Ni/NiO<sub>x</sub>/NiFe-LDH electrodes for MS analysis were obtained using the impedance-potential mode of the Zahner Zennium electrochemical workstation at 1 KHz in the dark, which is related to the equation<sup>3</sup>

$$\frac{1}{C^2} = \frac{2}{qN_D 2A^2 \epsilon_0 \epsilon_r} (V - V_{fb} - \frac{k_B T}{q})$$

where,  $C$  is the reverse-bias dependent differential capacitance,  $q$  is the charge of an electron ( $1.6 \times 10^{-19}$  C),  $N_D$  is the donor concentration in the semiconductor,  $A$  is the surface area of the electrode,  $\epsilon_0$  is the permittivity of vacuum,  $\epsilon_r$  is the relative permittivity,  $V$  is the applied potential in RHE,  $V_{fb}$  is the flatband potential,  $k_B$  is the Boltzmann's constant, and  $T$  is the temperature in Kelvin. The  $x$ -intercept of the linear region of the MS plot is indicative of the flatband potential  $V_{fb}$ .

### Electrochemical impedance spectroscopy (EIS)

The EIS spectra of the photoanodes performed at 1.23 V versus RHE in the range of 0.1 Hz to 100 KHz with an AC amplitude of 10 mV for the water oxidation. Their Nyquist plots data were analyzed by fitting to an equivalent electronic circuit model consisted of circuit elements as shown in the inset of Fig. 5b using the ZSimpWin software. Here,  $CPE_1$  and  $CPE_2$  represent constant phase elements,  $R_s$  represents the series and solution resistances, while  $R_1$  and  $R_2$  represent the charge transfer resistances at the photoanode/electrolyte interface and in the photoanode bulk, respectively.<sup>3,4</sup> The first semicircle on the left appeared at the high-frequency region corresponds to  $R_1$ , while the second semicircle on the right at the low-frequency region corresponds to  $R_2$ . For the  $n^+p$ -Si/SiO<sub>x</sub>/Ni/NiFe-LDH photoanode without activation of Ni,  $R_1$  and  $R_2$  are about 28 and 1.8  $\Omega$ , respectively. These values are about 7 and 1.8 times as large as those of the  $n^+p$ -Si/SiO<sub>x</sub>/Ni/NiO<sub>x</sub>/NiFe-LDH photoanode with the activated Ni/NiO<sub>x</sub> interface layer (4 and 1  $\Omega$ , respectively).

### Photovoltage Test

The photovoltage of the photoanode was determined by the potential difference between the catalyst layer coated on  $n^+p$ -Si/SiO<sub>x</sub> under illumination and on metallic  $p^{++}$ -Si/SiO<sub>x</sub> in the dark. The J-V test of the metallic  $p^{++}$ -Si/SiO<sub>x</sub> coated with the catalyst layer as an anode in dark is an electrocatalytic process;

while it is a photoelectrocatalytic process for that of n<sup>+</sup>p-Si/SiO<sub>x</sub>/Ni/NiO<sub>x</sub>/NiFe-LDH under illumination is. Since the coated catalyst is same on the metallic p<sup>++</sup>-Si/SiO<sub>x</sub> and n<sup>+</sup>p-Si/SiO<sub>x</sub>, the J-V curve shift is caused by the thermodynamic contribution, that is, the effect of generated photovoltage under illumination.<sup>5-7,29</sup>

### **Analysis of factors in influencing the photocurrent onset potential ( $V_{on}$ )**

In a PEC cell, the maximum theoretical photovoltage ( $V_{ph-max}$ ) for an anode is given by:<sup>8</sup>

$$V_{ph-max} = E^0(O_2/H_2O) - V_{fb} \quad (S1)$$

If there is a potential drop across the Helmholtz layer ( $\eta_H$ ) of the electrode, the photovoltage  $V_{ph}$  is determined by the relationship:

$$V_{ph} = E^0(O_2/H_2O) - V_{fb} - \eta_H \quad (S2)$$

The quantity  $V_{on} - V_{fb}$  is often referred to as overpotential ( $\eta$ ),<sup>9,10</sup> including both the kinetic overpotential,  $\eta_k$ , and the potential drop across the Helmholtz layer,  $\eta_H$ , for the OER<sup>11,12</sup>. That is:

$$V_{on} = V_{fb} + \eta = V_{fb} + \eta_H + \eta_k \quad (S3)$$

Combining Equation (S2) and (S3), the following relationship is given as:

$$V_{on} = \eta_k - V_{ph} + E^0(O_2/H_2O) \quad (S4)$$

Therefore,  $\eta_k$  and  $V_{ph}$  are two important factors in influencing  $V_{on}$ .

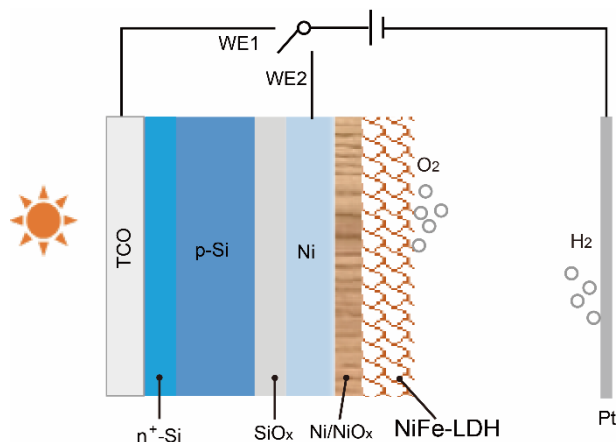


**Figure S1.** PEC device and wiring schematic with the n<sup>+</sup>p-Si/SiO<sub>x</sub>/Ni/NiO<sub>x</sub>/NiFe-LDH as a photoanode. The WE1 circuit connecting the wire to TCO was used to test the PEC properties as commonly reported. The WE2 circuit connecting the wire to Ni was used to electrodeposit NiFe-LDH with the homogeneous and high-performance film. In contrast, a larger applied bias and illumination were required for deposition of NiFe-LDH using the WE1 circuit and the obtained catalyst film was discontinuous and has worse performance because of the existence of the n<sup>+</sup>p-Si junction. Therefore, the facile and effective electrodeposition of NiFe-LDH using the Ni film as a working electrode was adopted in our experiment.

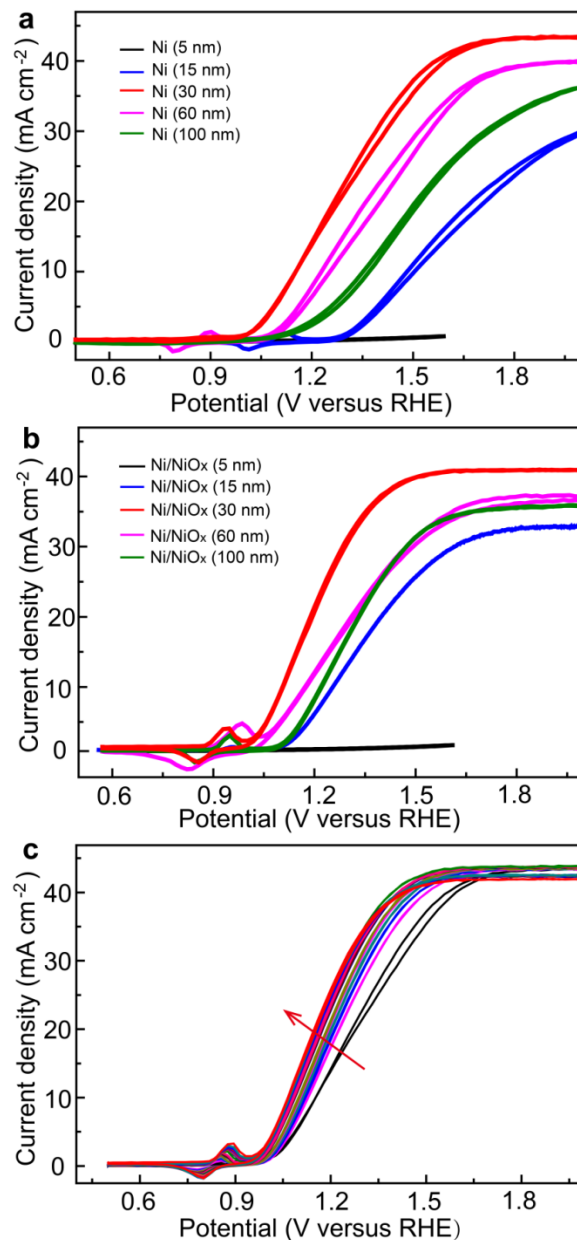


**Figure S2.** PEC performance optimization of the anodes. Ni film thickness dependent PEC performance on the n<sup>+</sup>p-Si/SiO<sub>x</sub> photoanodes (a) before and (b) after activation. (c) The PEC performance of twenty consecutive CV cycles for the 30-nm Ni coated n<sup>+</sup>p-Si/SiO<sub>x</sub>. The direction of the red arrow represents the gradual evolution of the PEC performance of the photoanode.

First, the Ni metal films with different thicknesses (5, 15, 30, 60 and 100 nm) were thermally deposited on the p-side surface of n<sup>+</sup>p-Si with native SiO<sub>x</sub> layer. The Ni film thickness dependent PEC performance of the n<sup>+</sup>p-Si/SiO<sub>x</sub>/Ni photoanodes demonstrates that the 30-nm thickness corresponds to the best PEC performance with the lowest onset potential and the highest saturated photocurrent density



for the first CV scan (Figure S2a). Then, the surfaces of these Ni films were partially activated during twenty consecutive CV cycles using a PEC three-electrode system in 1.0 M KOH solution. The activation results show that the photoanode deposited with 30-nm Ni again presents the best performance (Figure S2b). The gradual evolution of the PEC performance during the activation process for the representative 30-nm Ni coated  $n^+p$ -Si/SiO<sub>x</sub> photoanode is shown in Figure S2c. With consecutive CV scanning, the PEC activity of this anode gradually increases and then stabilizes after twenty cycles with an onset potential of ~0.965 V and a current density of ~23.6 mA cm<sup>-2</sup> at 1.23 V vs. RHE.

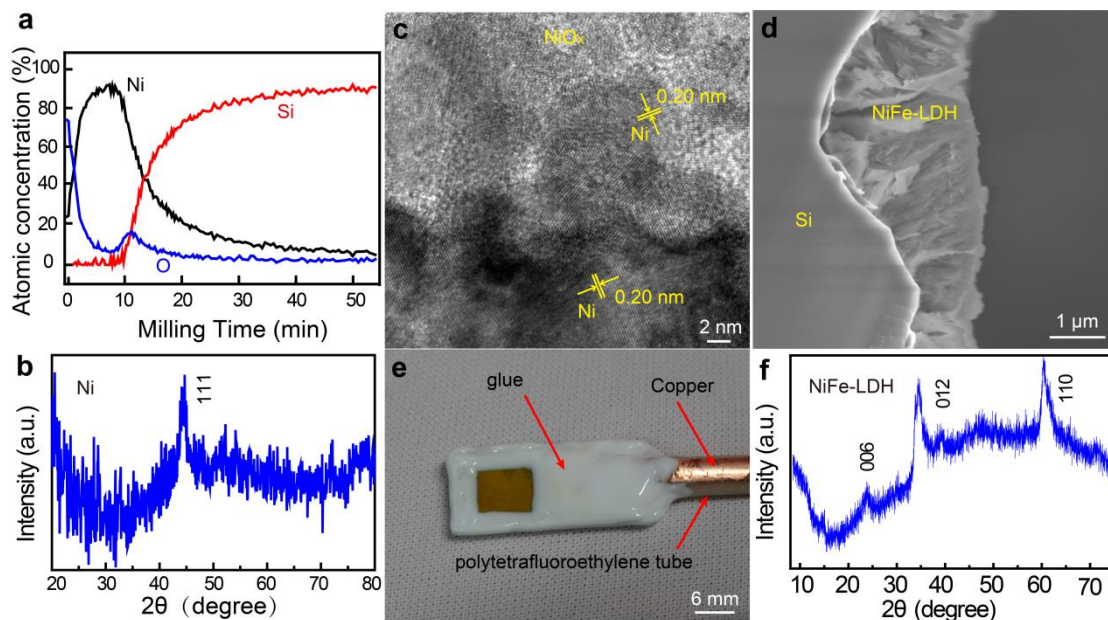


**Figure S3.** Structure and morphology characterizations of the designed photoanode. (a) Auger electron spectroscopy depth profiling of the surface of  $n^+p$ -Si/SiO<sub>x</sub>/Ni/NiO<sub>x</sub>. (b) XRD spectrum and high-resolution TEM image of Ni/NiO<sub>x</sub> on  $n^+p$ -Si/SiO<sub>x</sub>. (c) The amorphous NiO<sub>x</sub> layer encasing the Ni particles is formed on the Ni film. (d) The side-view SEM image and (e) digital photograph of the  $n^+p$ -Si/SiO<sub>x</sub>/Ni/NiO<sub>x</sub>/NiFe-LDH photoelectrode. (f) XRD pattern of NiFe-LDH on  $n^+p$ -Si/SiO<sub>x</sub>/Ni/NiO<sub>x</sub>.

The Auger electron spectroscopy (AES) depth profiling of the anode was performed after the Ni film activation using Ar ion milling (Figure S3a). The data show that the Ni and O signals appear on the surface of the photoanode. The peak of Ni appears at ~9 min of ion milling and the O signal decreases with increasing the Ni concentration, meaning the ratio of Ni/O increases. With the milling time further increases, a peak of the O signal appears at ~11 min of ion milling, and the Si signal increases continuously with the appearance of the peak of O, demonstrating the existence of the native SiO<sub>x</sub> layer. The (111) plane of Ni phase of the XRD pattern (Figure S3b) corresponds to the lattice distance of 0.20 nm in the high-resolution TEM image measured for the activated Ni film, and the amorphous NiO<sub>x</sub> layer encasing the Ni particles on the Ni film was observed after activation (Figure S3c).

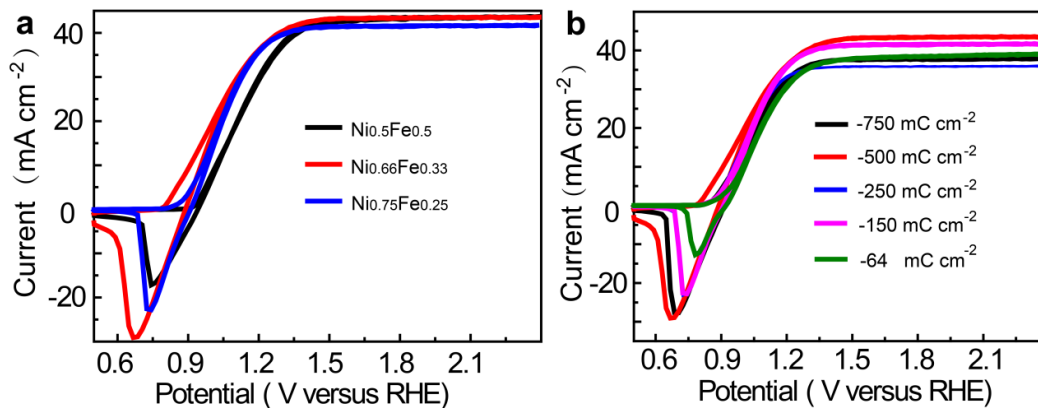


**Figure S4.** Performance optimization of NiFe-LDH. (a) CV curves of the n<sup>+</sup>p-Si/SiO<sub>x</sub>/Ni/NiO<sub>x</sub>/NiFe-LDH photoelectrodes under illumination with different Ni and Fe contents (Ni<sub>0.5</sub>Fe<sub>0.5</sub>, Ni<sub>0.66</sub>Fe<sub>0.33</sub>, Ni<sub>0.75</sub>Fe<sub>0.25</sub>) in the precursors, and Ni<sub>0.66</sub>Fe<sub>0.33</sub> shows the best performance. (b) CV curves of the n<sup>+</sup>p-Si/SiO<sub>x</sub>/Ni/NiO<sub>x</sub>/NiFe-LDH photoelectrodes under illumination with different thicknesses of the NiFe-LDH overlayer corresponding to different charges passed through the electrode (from -64 to -750 mC cm<sup>-2</sup>) with the optimal molar ratio of Ni:Fe (Ni<sub>0.66</sub>Fe<sub>0.33</sub>) during the electrodeposition at the applied cathodic potential of -1.0 V versus SCE.

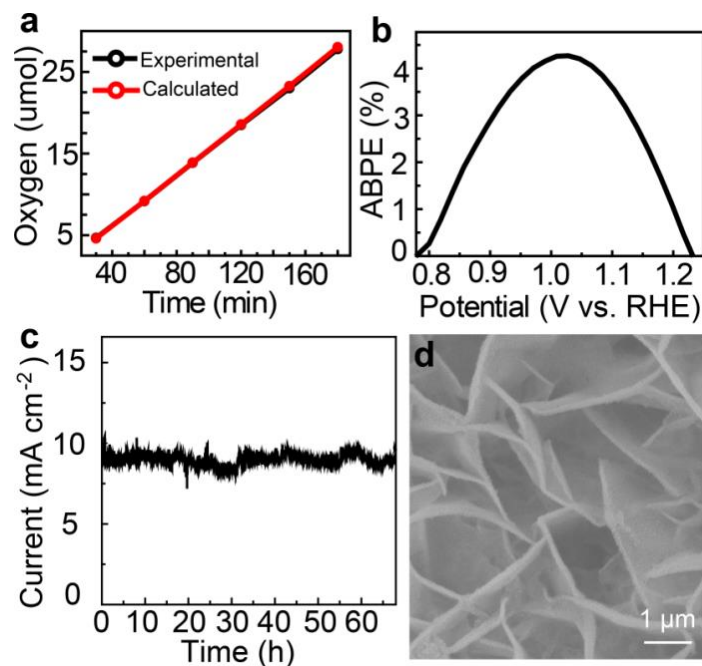


**Figure S5.** (a) O<sub>2</sub> production measured for the n<sup>+</sup>p-Si/SiO<sub>x</sub>/Ni/NiO<sub>x</sub>/NiFe-LDH photoanode under illumination in 1.0 M KOH (black line), and O<sub>2</sub> production calculated based on the charge passed assuming 100% Faradaic efficiency (red line). (b) The ABPE of the n<sup>+</sup>p-Si/SiO<sub>x</sub>/Ni/NiO<sub>x</sub>/NiFe-LDH photoanode. (c) Photocurrent as a function of time (J-t) reveals the stable performance of the n<sup>+</sup>p-Si/SiO<sub>x</sub>/Ni/NiO<sub>x</sub>/NiFe-LDH photoelectrode. (d) SEM image of NiFe-LDH on the surface of n<sup>+</sup>p-Si/SiO<sub>x</sub>/Ni/NiO<sub>x</sub>/NiFe-LDH after the stability test.

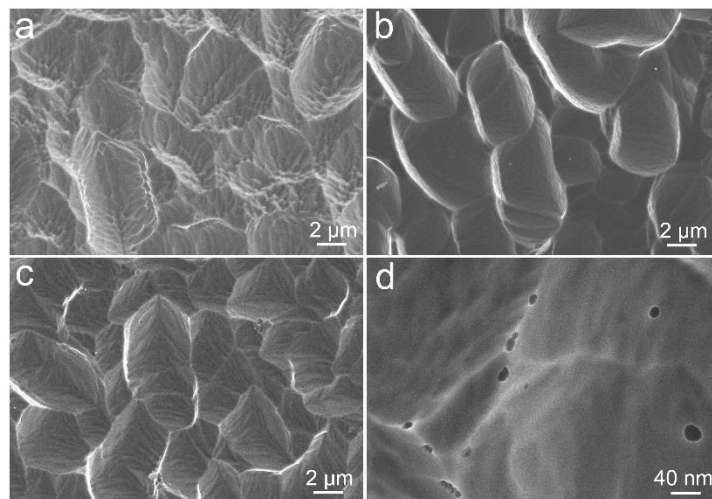


**Figure S6.** The morphology comparison of the polycrystalline Si substrate before and after the stability test. (a) The SEM image of the bare textured  $n^+p$ -Si/SiO<sub>x</sub> substrate. (b) The  $n^+p$ -Si/SiO<sub>x</sub>/Ni/NiO<sub>x</sub> substrate with a smoother surface compared to  $n^+p$ -Si/SiO<sub>x</sub>. (c) The Si surface after the stability test and removing NiFe-LDH and Ni/NiO<sub>x</sub> by diluted hydrochloric acid basically keeps intact. (d) The zoomed-in image of (c) displays a small amount of nanoscale etch pits on Si, but all its PEC activity was able to retain in the next round of the stability test.

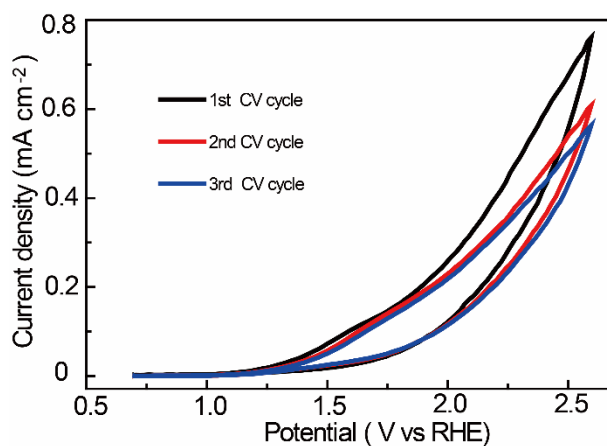


**Figure S7.** PEC performance of the bare  $n^+p$ -Si anode. Three successive CV scans of  $n^+p$ -Si under illumination indicate the poor PEC performance with the onset potential of around 1.1 V versus RHE and the current density of  $\sim 0.01 \text{ mA cm}^{-2}$  at 1.23 V versus RHE and the rapid decay.

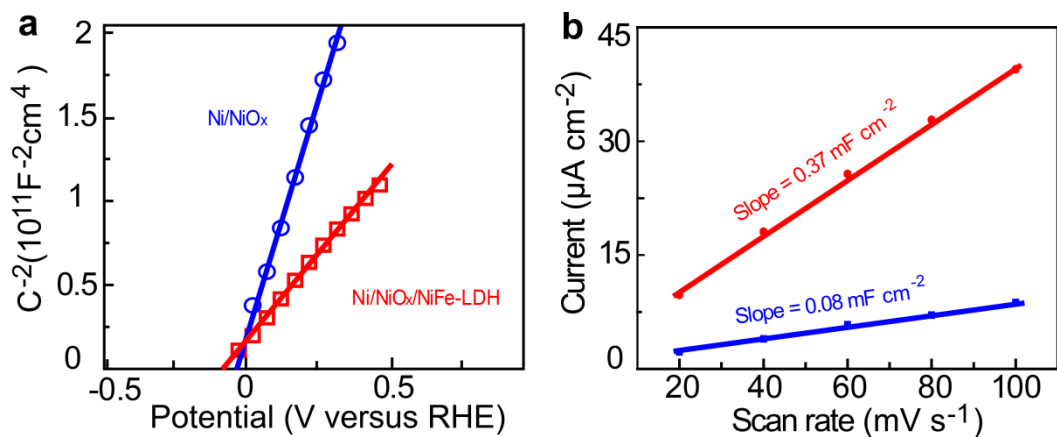


**Figure S8.** Mott-Schottky plots and electrochemical active surface areas. (a) MS plots of the Ni/NiO<sub>x</sub>/NiFe-LDH (red line) and Ni/NiO<sub>x</sub> (blue line) coated n<sup>+</sup>p-Si/SiO<sub>x</sub> photoanodes. (b) Capacitive currents at different scan rates for n<sup>+</sup>p-Si/SiO<sub>x</sub>/Ni/NiO<sub>x</sub>/NiFe-LDH (red line) and n<sup>+</sup>p-Si/SiO<sub>x</sub>/Ni/NiO<sub>x</sub> (blue line), respectively. The linear slope, equivalent to twice of the double-layer capacitance  $C_{dl}$ , is used to represent the ECSA.

It should also be noted that the layered structure and open-channels of NiFe-LDH might make some parts of the underneath NiO<sub>x</sub> exposed to the electrolyte to decrease the OER overpotential in n<sup>+</sup>p-Si/SiO<sub>x</sub>/Ni/NiO<sub>x</sub>/NiFe-LDH as a co-catalyst. But, the catalytic contribution of NiO<sub>x</sub> is smaller because of its inferior activity compared to NiFe-LDH and less exposed surface active sites due to the coverage of the thick NiFe-LDH. The scan-rate dependent electrochemical double-layer charge capacitance evaluated from CV scans of n<sup>+</sup>p-Si/SiO<sub>x</sub>/NiO<sub>x</sub>/NiFe-LDH is  $0.37 \text{ mF cm}^{-2}$ , which is about 4.6-fold as large as that of n<sup>+</sup>p-Si/SiO<sub>x</sub>/NiO<sub>x</sub> ( $0.08 \text{ mF cm}^{-2}$ ). This data also proves that the possible catalytic contribution of NiO<sub>x</sub> could be minor.

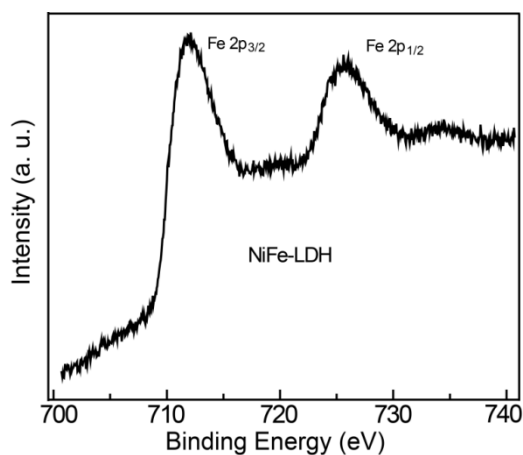


**Figure S9.** XPS spectrum of Fe 2p. High-resolution XPS spectrum of Fe 2p for the  $n^+p$ -Si/SiO<sub>x</sub>/Ni/NiO<sub>x</sub>/NiFe-LDH photoelectrode. Two dominant peaks of Fe 2p<sub>3/2</sub> at 711.7 eV and Fe 2p<sub>1/2</sub> at 725.5 eV observed in the Fe 2p XPS spectra as expected for this material indicate the existence of the Fe<sup>3+</sup> state in the NiFe-LDH layered arrays. Incorporation of Fe through a Ni-Fe partial charge-transfer activation process might enhance the OER activity.<sup>1,13,14</sup>

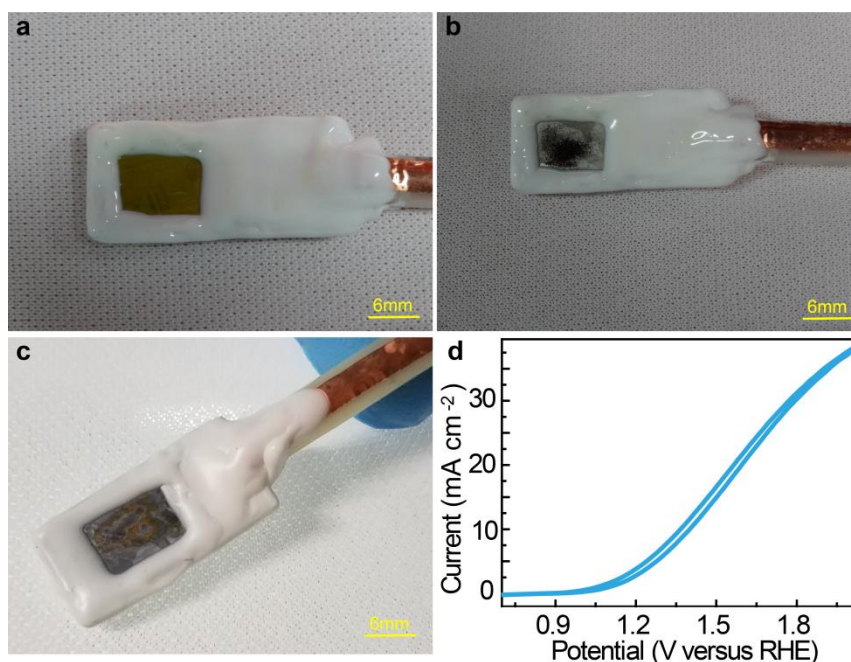


**Figure S10.** The photoanodes without a complete Ni/NiO<sub>x</sub> interlayer. Digital images of the n<sup>+</sup>p-Si/SiO<sub>x</sub>/Ni/NiFe-LDH photoanode (a) before and (b) after the first CV sweep. Most of NiFe-LDH on the surface starts to peel off after the first CV scan. This result indicates that Ni can act as an interlayer between Si and NiFe-LDH to ensure the stability of the anode and to afford good PEC performance in comparison to Ni/NiO<sub>x</sub>. The sample color changes from yellow to black, indicating the oxidation of Fe<sup>2+</sup> to Fe<sup>3+</sup> during the PEC test. (c) Digital image of the n<sup>+</sup>p-Si/SiO<sub>x</sub>/NiFe-LDH photoanode, showing that NiFe-LDH is difficult to be deposited on the surface of the n<sup>+</sup>p-Si/SiO<sub>x</sub> anode without the Ni/NiO<sub>x</sub> bridging layer.<sup>15</sup> (d) The CV curve of the n<sup>+</sup>p-Si/SiO<sub>x</sub>/NiFe-LDH photoanode with an onset potential of ~1.1 V versus RHE, and a current density of ~5 mA cm<sup>-2</sup> at 1.23 V versus RHE.



**Table S1. Water Oxidation Performance Comparison of Crystalline Si-Based Photoanodes**

Photoanode	Onset potential (V vs. RHE)	Photocurrent density at water oxidation potential (mA cm <sup>-2</sup> )	Saturation photocurrent density (mA cm <sup>-2</sup> )	Stability	Photovoltage (mV)	Fabrication method	Irradiation conditions	Ref.
n <sup>+</sup> p-Si/SiO <sub>2</sub> /Ni/a-Ni/NiFe-LDH	0.78 ± 0.02	37 ± 2	~41	68 h 1 M KOH	608	Successive CV potential cycling & EC deposition	Simulated AM 1.5 G (1-sun)	<b>Our work</b>
Si/Graphene/TiO <sub>2</sub> /FeNiCoO <sub>x</sub>	1	~7	~19	6 h 1 M NaOH	420	CVD, ALD, spin coating	AM 1.5 (100 mW cm <sup>-2</sup> )	16
n <sup>+</sup> p-Si/SiO <sub>2</sub> /NiFe Alloy	0.89	30.7	30.7	13 h 1 M KOH	620	Electrodeposition	1-sun simulated solar	3
n-Si/Ni NPs	1.1	~3.5	33	10 h 1 M NaOH	500	Electrodeposition	AM 1.5 G	17
Ni <sub>80</sub> Fe <sub>20</sub> /TiO <sub>2</sub> /n-Si	1.06	21.5	33	10 h 1 M KOH	500	Electrodeposition	AM 1.5 G	18
n-Si/SiO <sub>2</sub> /Al <sub>2</sub> O <sub>3</sub> /Pt/Ni	0.997	19.2	28.5	200 h 1 M KOH	490	ALD & RF sputtering	Simulated AM1.5 solar (100 mW cm <sup>-2</sup> )	5
n-Si/GO/CNTs/Graphene	~1.23	1	8	17 min 1 M KOH	-	Langmuir-Blodgett	AM 1.5 (1-sun)	19
n <sup>+</sup> pp <sup>+</sup> /Si/Co/NiCoO <sub>x</sub>	~1	21	21	6 days 1 M KOH	510	Sputtering	AM 1.5 G/λ > 635 nm)/1000 W Xe Lamp	20
n <sup>+</sup> p-Si/SiO <sub>2</sub> /TiO <sub>2</sub> /Ir	~0.95	~2.6	-	-	630	ALD	AM 1.5 G (1-sun) simulated solar	21
n-Si/CoO <sub>x</sub>	1.024 ± 0.2	22.9 ± 1.6	27	2500 h 1 M KOH	570	ALD	AM 1.5 G (1-sun) 100 W Xe Lamp	6
np <sup>+</sup> -Si/NiCo <sub>2</sub> O <sub>4</sub> /NiFe	0.95	> 25	33	72 h 1 M KOH	-	Reactive sputtering	AM 1.5 G (1-sun) simulated solar	22

n-Si/SiO <sub>2</sub> /Co/CoOOH	~1.52	0	35	2 h 1 M KOH	470	Electrodeposition	Simulated AM 1.5G	23
np <sup>+</sup> -Si/NiO <sub>x</sub>	1.05 ± 0.2	29 ± 0.8	~33	1200 h 1 M KOH	-	Sputtering	AM 1.5 G (1-sun)	24
np <sup>+</sup> -Si NiO <sub>x</sub>	0.95	20.7 ± 5	29	~36 h 1 M KOH	-	Sputtering	(1-sun) simulated solar	25
p <sup>+</sup> n-Si/Iron treated NiO	1.05	~16.5	~19	300 h 1 M KOH	500	Sputtering	38.6 mW/cm <sup>2</sup> λ > 635 nm	26
CoO <sub>x</sub> /p <sup>+</sup> n-Si	1	17	30	24 h 1 M KOH	610	Plasma enhanced ALD	(1-sun)/ 150 W Xe Lamp	27
np <sup>+</sup> -Si/TiO <sub>2</sub> /Ni	~1	~13	33.6	> 100 h 1 M KOH	520	ALD	AM 1.5 G (1-sun) /100 W Xe Arc Lamp	7
p <sup>+</sup> n-Si/Ir/IrO <sub>2</sub>	0.93	13.8	23	18 h 1 M H <sub>2</sub> SO <sub>4</sub>	500	Sputtering	38.6 mW/cm <sup>2</sup> /λ >635 nm/ 150 W Xe Lamp	28
n-Si/SiO <sub>2</sub> /Ni/NiO <sub>x</sub>	~1.07	12	~56	12 h 1 M KOH	500	Electron beam evaporation	AM 1.5 G (2-sun) /150 W Xe Lamp	29
Si/SiO <sub>2</sub> /TiO <sub>2</sub> /Ir	~1.03	~16	~26	8 h 1 M NaOH	510-570	ALD	AM 1.5 G (1-sun) simulated solar	30

## References

- (1) Li, Z.; Shao, M.; An, H.; Wang, Z.; Xu, S.; Wei, M.; Evans, D. G.; Duan, X. *Chem. Sci.* **2015**, *6*, 6624-6631.
- (2) Song, F.; Hu, X. L. *Nat. Commun.* **2014**, *5*, 4477.
- (3) Yu, X.; Yang, P.; Chen, S.; Zhang, M.; Shi, G. *Adv. Energy Mater.* **2017**, *7*, 1601805.
- (4) Zhang, H.; Ding, Q.; He, D.; Liu, H.; Liu, W.; Li, Z.; Yang, B.; Zhang, X.; Leia, L.; Jin, S. *Energy Environ. Sci.* **2016**, *9*, 3113-3119.
- (5) Digdaya, I. A.; Adhyaksa, G. W.; Trześniewski, B. J.; Garnett, E. C.; Smith, W. A. *Nature Commun.* **2017**, *8*, 15968.
- (6) Zhou, X.; Liu, R.; Sun, K.; Papadantonakis, K. M.; Brunschwig, B. S.; Lewis, N. S. *Energy Environ. Sci.* **2016**, *9*, 892-897.
- (7) Hu, S.; Shaner, M. R.; Beardslee, J. A.; Lichterman, M.; Brunschwig, B. S.; Lewis, N. S. *Science* **2014**, *344*, 1005-1009.
- (8) Walter, M. G.; Warren, E. L.; McKone, J. R.; Boettcher, S. W.; Mi, Q.; Santori, E. A.; Lewis, N. S. *Chem. Rev.*, **2010**, *110*, 6446-6473.
- (9) Barroso, M.; Pendlebury, S. R.; Cowan, A. J.; Durrant, J. R. *Chem. Sci.* **2013**, *4*, 2724-2734.
- (10) Iandolo, B.; Zhang, H.; Wickman, B.; Zorić, I.; Conibeer, G.; Hellman, A. *RSC Adv.* **2015**, *5*, 61021-61030.
- (11) Pleskov, Y. V. *Solar Energy Conversion: A Photoelectrochemical Approach*; Springer: New York, 1990; pp19-28.
- (12) Du, C.; Yang, X.; Mayer, M. T.; Hoyt, H.; Xie, J.; McMahon, G.; Bischoff, G.; Wang, D. *Angew. Chem. Int. Ed.* **2013**, *52*, 12692-12695.
- (13) Zhu, X.; Tang, C.; Wang, H.-F.; Zhang, Q.; Yang, C.; Wei, F. *J. Mater. Chem. A* **2015**, *3*, 24540-24546.
- (14) Xiao, C.; Li, Y.; Lu, X.; Zhao, C. *Adv. Funct. Mater.* **2016**, *26*, 3515-3523.
- (15) Ji, L.; Hsu, H.-Y.; Li, X.; Huang, K.; Zhang, Y.; Lee, J. C.; Bard, A. J.; Yu, E. T. *Nat. Mater.* **2017**, *16*, 127-131.
- (16) Li, C.; Xiao, Y.; Zhang, L.; Li, Y.; Delaunay, J.-J.; Zhu, H. *Sustainable Energy & Fuels*, DOI: 10.1039/c7se00504k.
- (17) Loget, G.; Fabre, Bruno.; Fryars, S.; Meriadec, C.; Ababou-Girard, S. *ACS Energy Lett.* **2017**, *2*, 569-573.
- (18) Cai, Q.; Hong, W.; Jian, C.; Li, J.; Liu, W. *ACS Catal.* **2017**, *7*, 3277-3283.
- (19) Yoon, K.; Lee, J.-H.; Kang, J.; Moody, M. J.; Hersam, M. C.; Lauhon, L. J. *Nano Lett.* **2016**, *16*, 7370-7375.
- (20) Bae, D.; Mei, B.; Frydendal, R.; Pedersen, T.; Seger, B.; Hansen, O.; Chorkendorff, I. *ChemElectroChem.* **2016**, *3*, 1546-1552.
- (21) Scheuermann, A. G.; Lawrence, J. P.; Kemp, K. W.; Ito, T.; Walsh, A.; Chidsey, C. E.; McIntyre, P. C. *Nat. Mater.* **2016**, *15*, 99-105.

- (22) Chen, L.; Yang, J.; Klaus, S.; Lee, L. J.; Woods-Robinson, R.; Ma, J.; Sharp, I. D. *J. Am. Chem. Soc.* **2015**, *137*, 9595-9603.
- (23) Hill, J. C.; Landers, A. T.; Switzer, J. A. *Nat. Mater.* **2015**, *14*, 1150-1155.
- (24) Sun, K.; McDowell, M. T.; Nielander, A. C.; Hu, S.; Shaner, M. R.; Yang, F.; Lewis, N. S. *J. Phys. Chem. Lett.* **2015**, *6*, 592-598.
- (25) Sun, K.; Saadi, F. H.; Lichterman, M. F.; Hale, W. G.; Wang, H. P.; Zhou, X.; Brunschwig, B. S. *PNAS* **2015**, *112*(12), 3612-3617.
- (26) Mei, B.; Permyakova, A. A.; Frydendal, R.; Bae, D.; Pedersen, T.; Malacrida, P. *J. Phys. Chem. Lett.* **2014**, *5*(20), 3456-3461.
- (27) Yang, J.; Walczak, K.; Anzenberg, E.; Toma, F. M.; Yuan, G.; Beeman, J.; Ager, J. W. *J. Am. Chem. Soc.* **2014**, *136*, 6191-6194.
- (28) Mei, B.; Seger, B.; Pedersen, T.; Malizia, M.; Hansen, O.; Chorkendorff, I.; Vesborg, P. C. *J. Phys. Chem. Lett.* **2015**, *5*, 1948-1952.
- (29) Kenney, M. J.; Gong, M.; Li, Y.; Wu, J. Z.; Feng, J.; Lanza, M.; Dai, H. *Science* **2013**, *342*, 836-840.
- (30) Chen, Y. W.; Prange, J. D.; Dühnen, S.; Park, Y.; Gunji, M.; Chidsey, C. E.; McIntyre, P. C. *Nat. Mat.* **2011**, *10*, 539-544.